ground water

Experimental Study of ERT Monitoring Ability to Measure Solute Dispersion

by Grégory Lekmine[1,2,3], Marc Pessel[1,3], and Harold Auradou[2,3,4]

Abstract

This paper reports experimental measurements performed to test the ability of electrical resistivity tomography (ERT) imaging to provide quantitative information about transport parameters in porous media such as the dispersivity α, the mixing front velocity u, and the retardation factor R_{f} associated with the sorption or trapping of the tracers in the pore structure. The flow experiments are performed in a homogeneous porous column placed between two vertical set of electrodes. Ionic and dyed tracers are injected from the bottom of the porous media over its full width. Under such condition, the mixing front is homogeneous in the transverse direction and shows an S-shape variation in the flow direction. The transport parameters are inferred from the variation of the concentration curves and are compared with data obtained from video analysis of the dyed tracer front. The variations of the transport parameters obtained from an inversion performed by the Gauss–Newton method applied on smoothness-constrained least-squares are studied in detail. While u and R_{f} show a relatively small dependence on the inversion procedure, α is strongly dependent on the choice of the inversion parameters. Comparison with the video observations allows for the optimization of the parameters; these parameters are found to be robust with respect to changes in the flow condition and conductivity contrast.

Introduction

The use of electrical resistivity tomography (ERT) to study near surface hydrogeological processes is a domain of active research. As resistivity depends on properties such as temperature, saturation, or solute concentration, this technique is now commonly used to monitor, for instance, saline intrusion (Bauer et al. 2006), solute transport (Bevc et al. 1991; Slater et al. 2000; Oldenborger et al. 2007; Monego et al. 2010; Wilkinson et al. 2010), and contaminated soil remediation (Labrecque et al. 1996). In recent years, laboratory-scale experiments have been performed in order to improve the ability to make and interpret ERT measurements. Various natural or modeled porous media were considered such as soil (Binley et al. 1996; West et al. 1999; Batlle-Aguilar et al. 2009), fractured (Labrecque et al. 2004), or stratified media (Slater et al. 2000).

In these previous studies, the ability of ERT to localize preferential flow paths or flow restrictions caused, for example, by clay layers or by fractures has been tested. With the improvement of the two dimensional (2D) or three dimensional (3D) inversion techniques, attempts were made to measure the tracer breakthrough curves on individual pixels (Binley et al. 1996; Olsen et al. 1999; Slater et al. 2000; Koestel et al. 2009). One of the main difficulties is the nonuniqueness of the ERT inversion problem. Ideally, the inversion may be constrained and coupling between the flow equation and the ERT data may be considered (Johnson et al. 2007; Pollock and Cirpka 2008). If this approach is not possible, a smoothness

---

[1] Laboratoire IDES, UMR 8148, Université Paris-Sud, Orsay, F-91405, France.

[2] Laboratoire FAST, UMR 7608, Université Pierre et Marie Curie-Paris 6 and Université Paris-Sud, Orsay, F-91405, France.

[3] CNRS, Orsay, F-91405, France.

[4] Corresponding author: Laboratoire FAST, UMR 7608, Université Pierre et Marie Curie-Paris 6 and Université Paris-Sud, Bât. 502, Orsay, F-91405, France; +33 1 69 15 80 84; harold.auradou@u-psud.fr

Received September 2010, accepted May 2011.

doi: 10.1111/j.1745-6584.2011.00837.x

constraint is typically applied. This may bias the ERT-inverted image which, in turn, may induce uncertainty in the transport parameters such as the tracer mean velocity (Singha and Gorelick 2006) or dispersivity (Vanderborght et al. 2005).

Usually, a variety of terms is added to the data misfit term in the objective function and their choice is often based on a priori information, guess, or user experience. The aim of this study is to investigate the influence of the regularization terms on the determination of the spatio-temporal transport of a solute.

To perform this study, a controlled laboratory-scale experiment was developed allowing for the injection of a more conductive fluid into a less conductive fluid initially saturating a homogeneous pack of beads poured into a Hele Shaw cell. Under our experimental conditions, the surface conductivity is negligible and the apparent conductivity is proportional to the fluid conductivity. The ERT imaging of the propagation of the second conductive fluid is done using electrodes placed on each lateral side of the porous medium. The injection condition is chosen such that the mixing front between the two fluids is correctly described by a one dimensional (1D) convection-dispersion equation.

The influence of the inversion parameters on the determination of the mean velocity of the front and its dispersivity is studied as function of various parameters. The second fluid is slightly dyed and the transport parameters are also inferred from the study of dye spreading. This measurement allows for the quantitative analysis of the parameter effects on the transport parameters obtained from the ERT. By repeating the experiments under various flow rates, we test the possibility to determine the evolution of the dispersivity and its dependence on the flow rate. The retardation factor associated to ion exchange between the fluid and the diffuse layer is also studied. Finally, the influence of the conductivity contrast on the evaluation of the transport parameters is considered.

Before explaining the experimental setup and procedure, we briefly describe the principle of the inversion and give an overview of the parameters which can be used to control the convergence.

ERT Principles

In the ERT method, electrical current is transmitted from one pair of electrodes and the electrical potential induced is measured at another pair of electrodes. This measurement is repeated by considering other pairs of electrodes and the large number of data sets acquired requires ERT data to be interpreted using an inverse algorithm.

Inverse modeling is usually performed by the Gauss–Newton method applied on a smoothness-constrained least-squares inversion (deGRoot-Hedlin and Constable 1990; Cardarelli and Fischanger 2006). It is based on the calculation of the sensitivity matrix for a homogenous half space, which is iteratively recalculated using a finite element method. In this study, the estimation of the vector of model parameters m^k at iteration k is optimized using the derived Robust constraint method of Loke and Barker (1996) applied to data and parameters by minimizing the objective function:

$$\boldsymbol{\varphi}(\mathbf{m}^{k+1}) = \mathbf{g}^{\mathrm{T}}\mathbf{W}_{\mathrm{d}}\mathbf{g} + \lambda(\mathbf{m}^k - \mathbf{m}^0)^{\mathrm{T}}\cdot\mathbf{C}^{\mathrm{T}}\mathbf{C}\cdot\mathbf{W}_{\mathrm{p}}(\mathbf{m}^k - \mathbf{m}^0) \quad (1)$$

where $\mathbf{g}$ is the data misfit vector, $\mathbf{W}_{\mathrm{d}}$ and $\mathbf{W}_{\mathrm{p}}$ are diagonal weighting matrices applied respectively to data and parameters, $\mathbf{C}$ is a roughness matrix, and $\mathbf{m}^0$ is the reference model. The objective function is iteratively recalculated to converge toward the global minimum, the model parameter vector $\mathbf{m}^k$ being updated such as:

$$\boldsymbol{\delta}\mathbf{m}^k = [\mathbf{J}^{\mathrm{T}}\mathbf{J} + \lambda\mathbf{W}_{\mathrm{p}}]^{-1}[\mathbf{J}^{\mathrm{T}}\mathbf{W}_{\mathrm{d}}\mathbf{g}(\mathbf{m}^k) - \lambda\mathbf{W}_{\mathrm{p}}(\mathbf{m}^k - \mathbf{m}^0)] \quad (2)$$

$\boldsymbol{\delta}\mathbf{m}^k = \mathbf{m}^{k+1} - \mathbf{m}^k$ is the perturbation vector of the model parameters, and $\mathbf{J}$ is the Jacobian sensitivity matrix. Equation 2 is a balance, weighted by the damping factor λ, between the least-squares and the steepest descent methods. In practice, the matrix $\mathbf{J}^{\mathrm{T}}\mathbf{J}$ is often near singularity and its inverse becomes unstable with divergent solutions (Lines and Treitel 1984). The damping factor λ controls the importance of the damping in and the inversion processes by controlling the variability of $\boldsymbol{\delta}\mathbf{m}^k$. Hence, high values of λ tend to reduce the size of $\boldsymbol{\delta}\mathbf{m}^k$, while a small λ leads to larger steps of $\boldsymbol{\delta}\mathbf{m}^k$ and may even induce singularity of the matrix to be inverted. Fixing λ to a high initial value, λ_{i}, and tuning it down between iterations allows to take advantage of the steepest descent (when λ is large) and least-squares methods (when λ tends to 0).

The damping factor also has an impact on the spatial resolution through $\lambda\mathbf{W}_{\mathrm{p}}$ (Equation 2) which is the ratio between λ and the calculated variance of each parameter of the reciprocal covariance matrix. High values in $\mathbf{W}_{\mathrm{d}}$ and $\mathbf{W}_{\mathrm{p}}$ (related to the errors on data and parameters) lower the weight of λ on the inversion processes which contributes to decrease the smoothing on the modeled resistivity contrasts.

With commercial software such as Res2Dinv, the minimization of the objective function is controlled by applying L_2 norms on data and parameters. Using L_1 norms on data and parameters enhances the constraint on inversion when measurement errors are nonnegligible. To reduce this artifact, an iterative reweighing of the matrices $\mathbf{W}_{\mathrm{d}}$ and $\mathbf{W}_{\mathrm{p}}$ is used such that a higher variance is assigned to the matrix when values of the difference $\mathbf{m}^k - \mathbf{m}^0$ overcome a certain cutoff factor (Wolke and Schwetlick 1988).

The interplay between the various parameters is complex and is done by the user on the basis of his own experience and the choice is often not discussed in publications. This work attempts to give a view of the influence of the damping parameter and norms and tries to give a recipe to guide the user in the choice of the parameters.

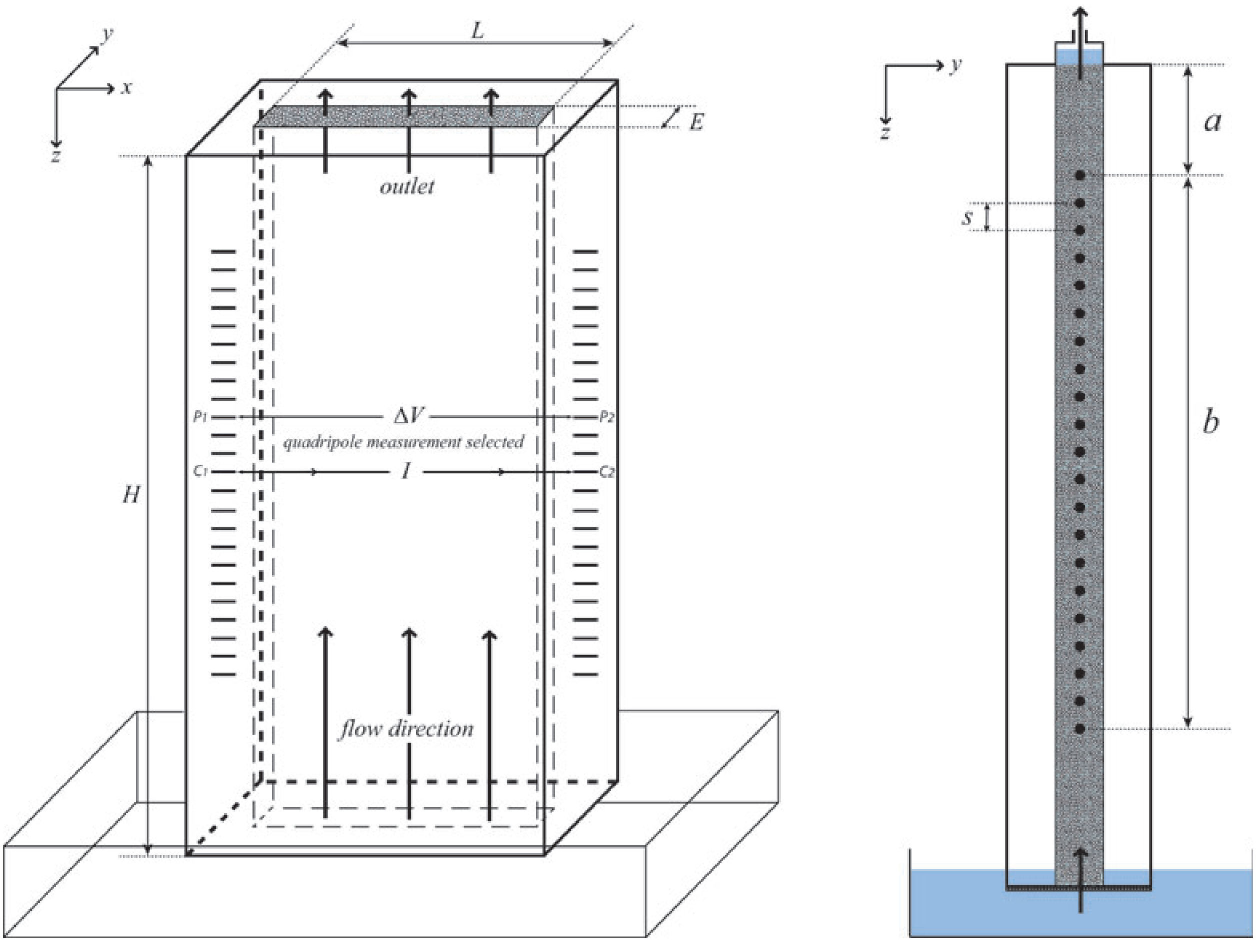

Figure 1. Schematic views of the experimental device. $H = 27.5$ cm, $L = 8.5$ cm, $E = 1$ cm. Right: Side view of the container during the pumping of the dyed fluid. The electrode spacing is $s = 1$ cm and the first and the last electrodes are separated by a distance $b = 20$ cm. The distance between the first (or last) electrode and the inlet (or outlet) of the medium is $a = 3.5$ cm.

Materials and Methods

Experimental Setup

The porous column is obtained by pouring spherical glass beads of diameters ranging between 125 and 166 μm into a transparent plexiglas container (Figure 1). The mean porosity of the bead packing is $\phi = 0.365$.

The container is positioned vertically (Figure 1) with the two vertical sides (corresponding to the container edges) sealed while the upper and lower edges are open. A nylon fabric of mesh size 100 μm is fixed on the lower side of the container. The fabric is used to support the glass bead pack while still enabling the fluid flow. The upper side is connected to a syringe pump sucking the fluids upward out of the column. The lower horizontal side dips into a bath which may be moved up and down. Before every experiment, the pore space is initially saturated by CO_2 and the medium is then saturated by the first fluid (fluid 1) from its lower part. In all experiments, fluid 1 is transparent and is obtained by dissolving a small amount of NaCl into pure degassed water. The second fluid contains a different quantity of NaCl together with 0.05 g/L of water blue dye (Acid Blue 22) adding an extra 15.5 μS/cm to the fluid conductivity. A calibration experiment was performed in order to determine the relation between the fluid conductivity σ_{f} in μS/cm and the salt concentration C in g/L. We found a linear relation: $\sigma_{\mathrm{f}} = bC + \sigma_{\mathrm{f}}^0$ with $b = 2 \times 10^3$ μSL/cm/g and $\sigma_{\mathrm{f}}^0 = 30$ μS/cm for measurements done at room temperature (i.e., 20°C).

The second fluid is then placed into the bath which is put back in contact with the lower side of the medium. The displacement experiment then starts by vertically pumping fluid 2. This injection procedure avoids unwanted intrusions while replacing a fluid by the other and allows one to purge completely the lower tank. In this way a perfectly straight front between the injected and displaced fluids is obtained at the onset of the experiment (Boschan et al. 2007).

The small density difference between the two fluids may influence the dispersion process and modify the dispersion coefficient. The gravity number $N_{\mathrm{g}} = k\mathbf{g}\Delta\rho/\mu u$—where k is the permeability of the medium (here about 14 Darcy), μ the water dynamic viscosity, and $\Delta\rho$ the density difference between the fluids 2 and 1—ranges in the present study between 1×10^{-3} and 6×10^{-3}; according to previous studies (Flowers and Hunt 2007) buoyant effects are thus sufficiently small.

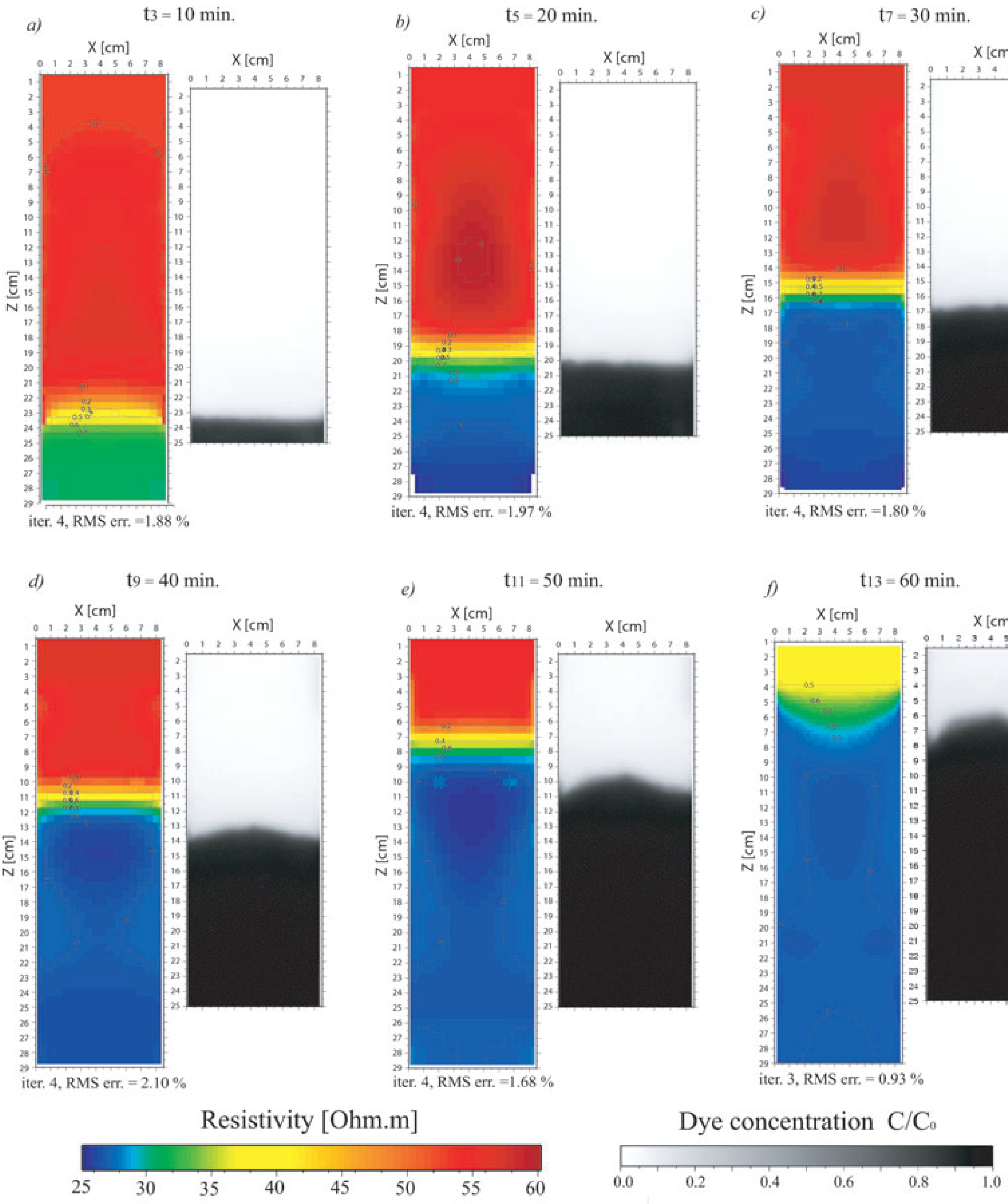

Figure 2. Time-lapse 2D ERT models produced from inversion of data sets of Experiment 13, associated to their corresponding gray level pictures provided by the video analysis.

The porous medium is placed between a light panel and a high resolution 12 bits digital camera. During the flow experiments, pictures of the porous medium are taken every 30 s. Reference images are also recorded before each experiment and after the full saturation by the dyed fluid. The relation between the local dye concentration C, the dye concentration in the input solution C_1, and the light intensities is initially determined from a set of calibration experiments where pictures were taken for several concentrations of the dye solutions (ranging between 0.05 and 0.1 g/L) saturating the porosity (Boschan et al. 2007). This procedure gives a 2D gray level distribution of the relative tracer concentration with a spatial resolution of 200 μm as shown in Figure 2.

ERT Measurement and Post-Processing

Two sets of 21 stainless steel screws of diameter 1.5 mm and separated by 10 mm are fixed along the two lateral edges of the container (Figure 1). Their ends are flattened and they are screwed until they penetrate by 2 mm into the bead pack. The first and the last screw of each vertical line are located, respectively, at 3.5 cm of both the lower and the upper openings of the container. These two vertical lines simulate ERT measurement conditions used in a borehole (Daily et al. 1991; Oldenborger et al. 2007).

Under these conditions, more than 3600 electrode configurations can be considered. A sensitivity analysis (Furman et al. 2007) adapted to our geometry confirmed that cross-borehole measurements are most appropriate to monitor the upward mixing front, particularly in the central part of the porous column. A sequence of 190 quadripoles in transverse dipole-dipole configuration (Figure 1) is chosen because of its higher relative sensitivity in the area between the electrodes representing boreholes. Data are acquired with a multielectrode system providing a temporal resolution of 5 min for the total acquisition of the 190 quadrupoles of every ERT time-step. For each acquisition a constant voltage $V_{\mathrm{ab}} = 12$ V is maintained during 250 ms. Prior to the current injection, a self-potential measurement is performed and removed from the electrical potential. During the acquisition, the mixing front continuously moves up into the porous medium. To reduce the temporal drift, we assumed that the mixing front evolves linearly with time and the values of the apparent resistivities for a set of measurements are modified according to:

$$\rho^{c}_{a(t_n)} = \left[\frac{\rho_{a(t_{n-1})} - \rho_{a(t_n)}}{\Delta t}.\tau\right] + \rho_{a(t_n)} \tag{3}$$

where $\rho^{c}_{a(t_n)}$ (Ω m) is the modified apparent resistivity, $\rho_{a(t_{n-1})}$ and $\rho_{a(t_n)}$ are the measurements acquired at the times t_{n-1} and t_n for the same set of electrodes, $\Delta t = t_{n-1} - t_n$ is the time between the repetition of the same measurement, and τ is the time elapsed since the beginning of the acquisition of the set n.

The logarithms of the modified apparent resistivities are, finally, inverted (see section ERT principles) with a constant reference model $\mathbf{m}^0$ and models produced from a 2D grid of 8.5 cm width and 28.0 cm height comprising 3816 (model 1) or 1026 cells (model 2). The mesh size is 0.25 cm for the first model and 0.5 cm for the second one. In both cases, the mesh is uniform from $z = 2.0$ to 27.0 cm depth. Near the boreholes the mesh size is refined to reduce sharp resistivity variations between adjacent cells (Nimmer et al. 2008). Res2DInv imposes Neumann's boundary conditions on the borehole edges and on the bottom part of the models, whereas Dirichlet's boundary conditions are imposed at the surface. These conditions are used by default in Res2DInv as they correspond to the boundary conditions found in the field. Yet, they do not correspond to the conditions at the lab scale: Indeed Dirichlet's condition on the lateral sides of the container should be considered. As we will show in the next paragraph, this drawback is partially removed by using a proper normalization of the resistivity measurements. The Jacobian matrix is recalculated at each iteration and the calculation is ended after seven iterations.

For all set of electrodes, the apparent resistivity measured before and after all the experiments (i.e., when the porous media is saturated by the fluid 1 or 2) is found to vary linearly with the resistivity of the fluid in the pore space. This linear behavior, which is equivalent to the Archie law with a formation factor related to the gradient, holds over the full range of fluid conductivities considered and demonstrates that the surface conductivity of the grains is negligible with respect to the fluid conductivity (Revil and Glover 1998). This observation is consistent with the results obtained by Leroy et al. (2008) who reported for an equivalent configuration and for the lowest fluid conductivity used here (Table 1 in Leroy et al. 2008) a Dukhin number (ratio between the surface and fluid conductivities) of the order of 0.08.

We took advantage of the linear relation between the fluid and the apparent resistivity to determine a formation factor, $F(x, z)$, for each cell:

$$F(x, z) = \frac{\rho^0_b(x, z)}{\rho_1}, \tag{4}$$

where ρ_1 is the resistivity of fluid 1 and $\rho^0_b(x, z)$ the resistivity in cell (x, z) obtained from the inversion of the initial data set (when the porosity is saturated by fluid 1). The fluid resistivity $\rho_{\mathrm{f}}(x, z, t)$ is thus related to the bulk resistivity $\rho_{\mathrm{b}}(x, z, t)$ by:

$$\rho_{\mathrm{f}}(x, z, t) = \frac{\rho_{\mathrm{b}}(x, z, t)}{F(x, z)}. \tag{5}$$

Thanks to the linear relation between the concentration C of dissolved NaCl and ρ_{f}, the local normalized concentration $c(x, z, t) = (C(x, z, t) - C_1)/(C_2 - C_1)$ is finally calculated where $C(x, z, t)$, C_1, and C_2 are, respectively, the local concentrations at time t and the NaCl concentration in fluids 1 or 2.

Figure 2 shows, for one experiment, the 2D relative concentration maps inferred from the video analysis together with the 2D maps of the ERT survey. Figure 3 shows the variation of the concentration along the vertical axis where the concentration $c(z)$ is obtained by averaging the normalized concentration $c(x, z, t)$ over the horizontal coordinates. The two concentration curves display an S shape as typically observed when a small amount of dissolved species is dispersed by flow in porous media (Bear 1972).

For a continuous injection of tracers at a constant concentration and under the assumption that the dispersion mainly occurs along the flow direction, the concentrations are solutions of the convection-dispersion equation and vary like:

$$c(z, t) = \frac{1}{2}\left[1 + \mathrm{erf}\left(\frac{z - \bar{z}}{2\sqrt{Dt}}\right)\right] \tag{6}$$

where $\bar{z}$ (cm) is the mean tracer front position at time t and D is the dispersion coefficient.

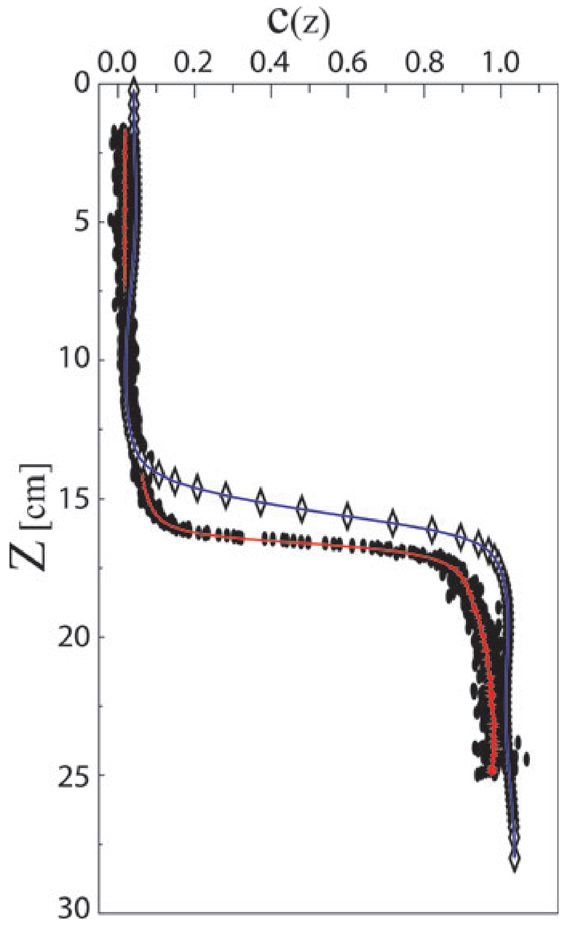

Figure 3. Vertical concentration $c(z)$ for time-step $t_7 = 30$ min (i.e., when the mean front is midway between the outlet and the inlet) from ERT (◇) and video analysis (●). Solid lines: fits by Equation 6.

The least-squares fit of $\bar{z}$ and D by Equation 6 is displayed by solid lines in Figure 3; we use this adjustment to determine the transport parameters. In this study, the dispersion coefficients are always found to be, at least, more than five times the typical molecular diffusion coefficient of the tracers; molecular diffusion has thus a negligible influence on the dispersion which is dominated by the velocity fluctuation at pore scale. In such regime, the transport is characterized by a constant dispersivity α with $\alpha = D/u$.

The fronts displayed in Figure 2 show a concave shape (the dye progresses faster at the center of the porous medium than along the sides). Its effect on the transport parameters are however relatively small. This was demonstrated by estimating the dispersivity and the mean velocity as function of the size of the horizontal window over which the concentration is averaged. Hence, when the window size was increased from one-eighth to one time the width of the porous medium, the dispersivity and the mean velocity were found to vary by, respectively, less than 5 and 2%. The finite width of the media has a small influence on the transport parameters and the flow can be considered as 1D.

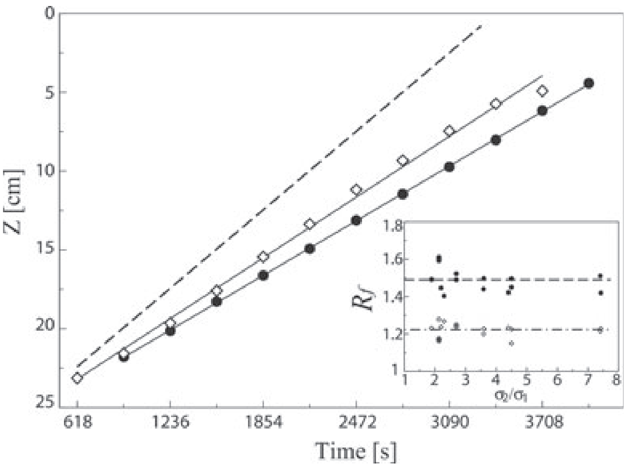

Figure 4. Evolution of the mean front position, Z, with time inferred from ERT (◇) and video analysis (●) for Experiment 13, values estimated from the pump velocity (dashed line). Inset: retardation factors R_f for 15 experiments (Table 1) as function of the fluid conductivity ratio σ_2/σ_1.

Results

Mean Front Position and Average Flow Velocity

Figure 4 displays the variation of the mean front positions as function of time, for both fronts, a linear increase of the average position with time is observed. Linear regressions show that the actual velocities are $u_{\mathrm{ERT}} = 6.4 \times 10^{-3}$ cm/s and $u_{\mathrm{dye}} = 5.4 \times 10^{-3}$ cm/s both lower than the average flow velocity $u = 8.1 \times 10^{-3}$ cm/s imposed by the pump.

This delay is quantified by the retardation factor R_{f} defined as the ratio between the fluid velocity u and the dissolved species velocity u_{dye} or u_{ERT}. The inset of Figure 4 shows R_{f} calculated for each of the experiments performed as function of the conductivity ratio σ_2/σ_1. We observed that the retardation factor is not influenced by the conductivity contrast and flow conditions. Average values are, respectively, 1.2 and 1.5 for the ERT and the video measurements with a standard deviation of 0.05.

An additional experiment was performed to confirm these observations. In this experiment, a dyed fluid was injected in the porous medium initially saturated by CO_2. Two fronts were observed, the first corresponding to the saturation of the medium by water and the second underlining the retarded progression of the dye. The two fronts were observed to progress at constant velocities with a retardation factor $R_{\mathrm{f}} = 1.55$. This latter value is close to the values inferred from the dispersion experiments presented in Figure 4.

Unfortunately, because of the exceedingly resistive contacts of the electrodes with the dry part of the porous medium, this air/water displacement experiment does not allow to determine the retardation factor associated to the ions. However, a recent work made by Peters et al. (1996) reports a NaCl retardation factor of $R_{\mathrm{f}} = 1.1$ for flow in a Berea's Sandstone and $R_{\mathrm{f}} = 1.04$ when the fluid is injected into an unconsolidated sand pack; these values are close to the value 1.2 ± 0.05 observed in our medium and were found robust with regard to changes of the inversion parameters.

Effect of the Robust Constraint Method (L_1 vs. L_2-norm)

Numerical results of Seaton and Burbey (2002) demonstrated that an L_2-norm inversion applied to data and/or parameters tends to smooth resistivity contrasts compared to the L_1-norm inversion. Inversion of our experimental data confirmed their observations: the smoothing results in an increase of the dispersion and the development of local artifacts. These effects can be reduced when a L_1-norm inversion is used. In Res2DInv, the L_1-norm inversion is performed by iteratively reweighing the expression of the least squares and by fixing a cutoff factor on the initial sets of data and parameters. Values outside the interval are reweighed by the recalculation of $\mathbf{W}_\mathrm{d}$ and $\mathbf{W}_\mathrm{p}$ (Equation 2) in order to minimize their weight in the next iteration. Figure 5 shows the vertical variations of the concentrations estimated for various cutoff factors applied on parameters, whereas a constant cutoff value of 0.05 is applied on the data. For cutoff factors above 0.01, a hollow and a hump appear respectively at the front and rear of the mixing front: in this case, the results are similar to the ones obtained with a L_2-norm. These artifacts fully disappear for values above 0.01, that is, when a L_1-norm is used.

Even if the side-slope effects lead to nonphysical negative values of the tracer concentration, it has a relatively limited effect on the slope of the dispersion front and, as a consequence, on the dispersion coefficient. Thus, for a factor of 0.1 (diamonds on Figure 7), the adjusted coefficient of dispersion is $D = 25 \times 10^{-5}$ cm^2/s, whereas for the lowest factors (+) we obtained $D = 19 \times 10^{-5}$ cm^2/s.

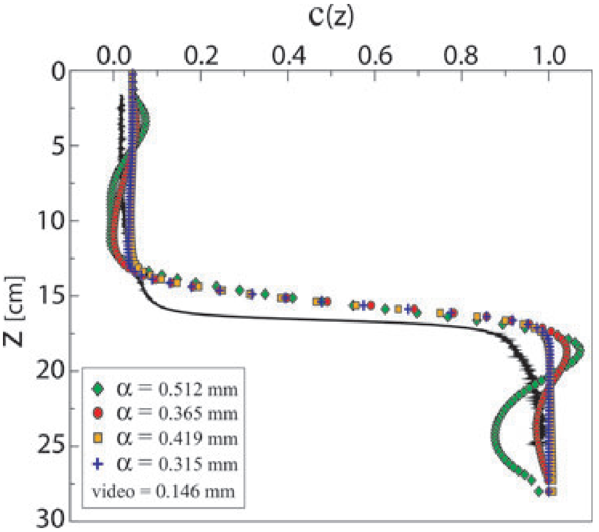

Figure 5. Effects of the Robust constraint method on the dispersion curve measured at time $t_7 = 30$ min for Experiment 13 (Table 1). Models are produced with cutoff factors, 0.1 (◇), 0.01 (●), 0.001 (□), 0.0001 (+), and the solid line shows the concentration variation obtained with the video measurement.

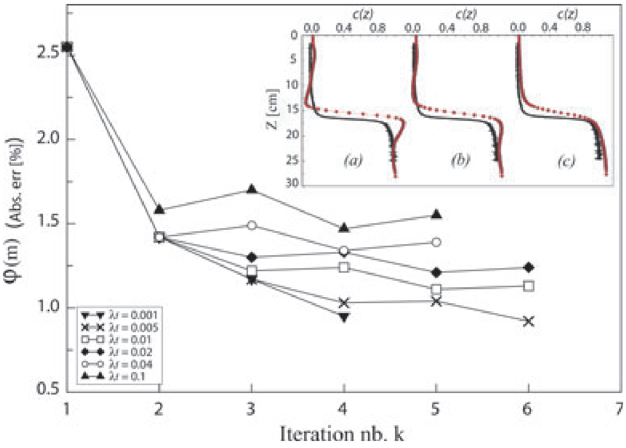

Figure 6. Objective function φ(m) as function of the iteration number k for $\lambda_\mathrm{i} = 0.1$ and various final damping factors such as, ▼, □, ×, ◆, ○, ▲ are $\lambda_\mathrm{f} = 0.001, 0.005, 0.01, 0.02, 0.04, 0.1$, respectively. Inset: Normalized concentrations $c(z)$ with (a) $\lambda_\mathrm{f} = 0.001$, (b) $\lambda_\mathrm{f} = 0.02$, and (c) $\lambda_\mathrm{f} = 0.1$.

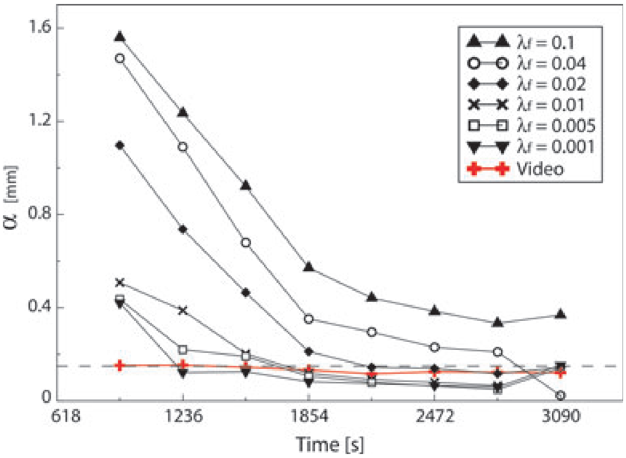

Figure 7. Dispersivity α as function of time inferred from time-lapse ERT modeling of Experiment 13, where (+) is the estimation of the video analysis and ▼, □, ×, ◆, ○, ▲ are $\lambda_\mathrm{f} = 0.001, 0.005, 0.01, 0.02, 0.04, 0.1$, respectively. The dashed horizontal line corresponds to a dispersivity $\alpha = 0.146$ mm.

Effect of the Damping Factors

The convergence of ERT models depends on the choice and the way λ is modified during the iterations. Variations of the perturbation vector $\boldsymbol{\delta}\mathbf{m}^k$ are usually bounded by a high initial value λ_i to avoid divergences of the solution due to possible errors in the data. Compared to field measurements, the noise level is assumed to be negligible allowing one to assign a low initial value $\lambda_\mathrm{i} = 0.1$. In this study, λ is divided by 2 between iterations until it reaches a fixed value λ_f. When this threshold is met, λ remains constant in the subsequent iterations. Figure 6 shows the convergence of the objective function $\boldsymbol{\varphi}(\mathbf{m}^k)$ for various λ_f.

For constant ($\lambda_\mathrm{f} = 0.1$) or high final values ($\lambda_\mathrm{f} = 0.04$), $\boldsymbol{\delta}\mathbf{m}^k$ is constrained to low variations which prevent $\boldsymbol{\varphi}(\mathbf{m}^k)$ to converge to the optimal set of ERT model parameters. Similarly when λ_f tends to 0.001 (triangle down on Figure 6) the steps $\boldsymbol{\delta}\mathbf{m}^k$ to the solution are important and only four iterations are needed to reach the optimal solution with $\boldsymbol{\varphi}(\mathbf{m}^k) = 0.95\%$. The inset of the Figure 6 shows the vertical variations of the concentrations estimated from ERT models at the fourth iteration for three values of λ_f (0.001, 0.02, and 0.1) together with results of the video analysis (black curve).

When λ_f tends to zero the inversion processes converges rapidly toward an optimal solution but produces humps and hollows on the front and rear of the front observed in Figure 5. Under these conditions, even if the cutoff factor tends to zero, these artefacts cannot be suppressed. The higher λ_f is the smoother are the hollow and the hump producing an artificial spreading of the mixing front. Its effect on the dispersivity is quantitatively illustrated in Figure 7. In addition to a significant decrease of the dispersivity with λ_f, the dispersivity tunes down with the upward tracer propagation and, finally, stabilizes to a constant value as function of λ_f.

If we refer to the absolute error of the objective function (Figure 6), the ERT models are more "reliable" for $\lambda_f = 0.0001$ and 0.0005. However, as shown in Figure 7, results for $\lambda_f = 0.02$ are much closer to the video analysis and converged very rapidly to this value as the tracers progress in the porous medium.

Variation of α with the Flow and Fluid Properties

Hereafter, the experimental data are inverted using the values inferred from the protocol described in the previous section. A robust constrain cutoff factor of 0.005 is applied on the model parameters and the damping factors are, respectively, fixed to $\lambda_i = 0.1$ and $\lambda_f = 0.02$.

Influence of the Conductivity Contrast

Experiments with constant flow and density contrast were performed (Experiments 5 to 9 and 13) in order to study the effect of the conductivity contrast on the dispersivity in this set of experiments, the amount of dissolved NaCl is gradually reduced so that their respective conductivity decreases while the density difference $\Delta\rho = 0.4$ g/L remains constant which provides a constant conductivity contrast around 750 µS/cm.

Under such experimental conditions, the dispersivity is expected to remain constant: this is indeed the case for the dispersivity obtained from the video analysis (solid circles in Figure 8). The electrical measurements give a similar result: the dispersivity coefficient is constant excepted when the conductivity contrast is below 2; in the latter case a marked increase of the dispersivity is observed.

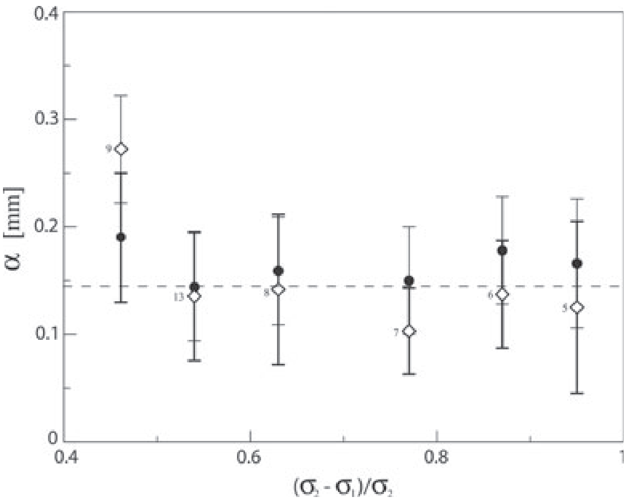

Figure 8. Dispersivity as function of the conductivity contrast $(\sigma_2 - \sigma_1)/\sigma_2$ deduced from ERT models (◇) and video analysis (●) for Experiments 5 to 9 and 13.

Influence of the Flow Rate

Experiments 12 to 15 (Table 1) were conducted with the same fluid properties but for various flow rates. Figure 9 shows the coefficient dispersion normalized by the molecular coefficient of dispersion, D_m, as function of the Péclet number $Pe = ua/D_m$ where a is the bead diameter. The coefficient D_m depends on the nature of the tracer; for Na^+ and Cl^-, we took $D_m = 1.6 \times 10^{-5}$ cm²/s, and for the dye $D_m = 0.65 \times 10^{-5}$ cm²/s. In this figure, D corresponds to the average value of $D(t)$ for times t large enough so that D has converged toward a constant value as shown by the Figure 7. The vertical bars in Figure 9 correspond to the standard deviation of $D(t)$ measured in the threshold regime.

Considering the entire range of Péclet number, the coefficient of dispersion inferred from ERT modeling (diamonds and triangles) are close to the values obtained with the video (filled circles) or found in the literature (solid line).

The inset shows the variation of the dispersivity with the Péclet number. They are close to the mean diameter of the grains used. We observed that the dispersivity measured by ERT has a slight tendency to increase with the flow velocity. Changing the mesh size while changing the damping parameters according to the procedure described previously, is also found to have a small influence on the dispersivity: a reduction by a factor 2 of the mesh results in a decrease of the dispersivity by about 40%.

Discussion

To guide our choice of the inversion parameters for our field measurements, we have performed laboratory experiments allowing for a quantitative comparison between the dispersivity inferred from ERT and video analysis.

The analysis of the vertical evolution of the mean fronts revealed that both tracers are absorbed: the absorption is characterized by a retardation factor independent of the flow and conductivity conditions. For all sets of inversion parameters (grid mesh size, norm applied, and damping parameters) the retardation parameters associated

Table 1
Experimental Setup and Procedure

	Fluid 1		Fluid 2					
$n°$	C_1 (g/L)	σ_1 (μS/cm)	C_2 (g/L)	c_{dye} (g/L)	σ_2 (μS/cm)	Q (mL/min)	$\Delta\rho$ (g/L)	N_g (x 10^{-3})
1	0.4	848	1.5	0.1	3100	1.5	1.2	6
2	0.2	438	0.95	0.05	1976	1.5	0.8	4
3	0.2	438	0.75	0.05	1573	1.5	0.6	3
4	0.4	842	0.9	0.1	1935	1.5	0.6	3
5	0.01	36	0.36	0.05	785	1.5	0.4	2
6	0.05	120	0.4	0.05	890	1.5	0.4	2
7	0.1	221	0.45	0.05	981	1.5	0.4	2
8	0.2	435	0.55	0.05	1177	1.5	0.4	2
9	0.4	841	0.75	0.05	1583	1.5	0.4	4
10	0.1	221	0.36	0.05	804	1.5	0.3	2
11	0.3	625	0.65	0.05	1370	0.5	0.4	6
12	0.3	625	0.65	0.05	1370	1.0	0.4	3
13	0.3	625	0.65	0.05	1370	1.5	0.4	2
14	0.3	625	0.65	0.05	1370	2.0	0.4	1
15	0.3	625	0.65	0.05	1370	2.5	0.4	1
16	0.2	438	0.95	0.05	1976	1.5	−0.8	−4
17	0.2	438	0.75	0.05	1573	1.5	−0.6	−3
18	0.05	120	0.4	0.05	890	1.5	−0.4	−2
19	0.2	435	0.55	0.05	1177	1.5	−0.4	−2
20	0.01	36	0.36	0.05	785	1.5	−0.4	−2
21	0.1	221	0.45	0.05	981	1.5	−0.4	−2
22	0.1	221	0.36	0.05	804	1.5	−0.3	−1
23	0.3	620	1.45	0.05	2545	1.5	1.2	6
24	0.3	630	1.05	0.05	2120	1.5	0.8	4
25	0.3	635	0.45	0.05	985	1.5	0.2	1

Notes: C_1 and C_2 are concentrations of NaCl dissolved in fluids 1 and 2; σ_1 and σ_2 are their related electrical conductivity; c_{dye} is the quantity of dye used to color fluid 2. Q is the flow rate, $\Delta\rho$ the density difference between fluids 2 and 1 and N_g is the gravity number defined in the paragraph.

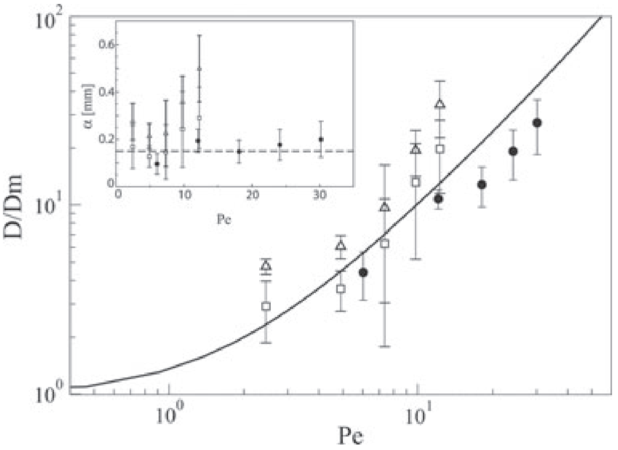

Figure 9. Normalized dispersion coefficient D/D_m as function of the Péclet number Pe for Experiments 12 to 15 compared with the theoretical curve of Bear (1972). (△) mesh size 106 × 36 cells, cutoff factor = 0.005, $\lambda_i = 0.1$ and $\lambda_f = 0.02$. (□) mesh size 54 × 19 cells, cutoff factor = 0.005, $\lambda_i = 0.1$ and $\lambda_f = 0.01$. (●) are deduced from video analysis. Inset: Same results expressed as dispersivity $\alpha = D/u$.

with the sorption of the sodium on the grains is estimated close to 1.2 ± 0.05 with a good precision over the whole window of conductivity contrasts. The ability of ERT to measure the retardation factor suggests that this technique may be used to determine isotherm adsorption of electrical tracers.

The value of the dispersivity is particularly sensitive to damping parameters. Low values of the final damping factor λ_f provide a limited dispersion but important artifacts above and below the mixing front while higher values give better fits. An increase of the damping parameter smoothes the mixing fronts but results in an overestimation of the dispersivity. The most reliable estimation of the dispersivity is not provided by ERT models having reached the lowest value of the objective function but depends on the appropriate association of λ_f and the cutoff factor. The comparison between ERT models and video analysis allows for the determination of an optimum set of parameters. For this set of parameters, the dispersivity varies only slightly with time: this is not the case for others set of parameters.

Consequently, the poor density of measurements associated with a local low sensitivity distribution contributes to smooth the modeled resistivity contrasts in the bottom area of the porous media increasing artificially α. Similar conclusion were drawn by Kemna et al. (2002) using numerical experiments. We observed that the set of parameters leading to the best estimation of the dispersivity is the one that shows the lowest sensitivity; for this set, the distance from the bottom required to reach a constant dispersivity is the lowest.

For a given set of inversion parameters, we found that the dispersivity (measured sufficiently far away from the bottom of the cell) is found to increase slightly with the flow velocity but is very robust with regard to the conductivity contrast between the fluids (providing a contrast lower that a factor 2) demonstrating the ability of the electrical measurement to determine the transport parameters.

For data obtained from field measurements, inversion parameters cannot be adjusted by comparison with a second method. Practically, the user first selects a grid, and then the type of norm applied. In case of poor quality of measurements or small data set compared to the number of parameters, a robust constraint method should be used with different cutoff factors in order to suppress artifacts that may appeared at the rear and the front of the mixing front. Finally, the damping factor is varied to avoid the inverse matrix singularity: the choice of this factor is not solely guide by a strict minimization of the objective function; we observed that a reduce fluctuation of the dispersivity with time is a good indicator to select the damping factor.

For the pack of beads used here, both techniques (ERT and Video) give a dispersivity very close to the bead diameter in agreement with data published in the literature (Bear 1972).

Conclusion

This experiment is an important and necessary step to demonstrate the ability of ERT to provide reliable information about the transport parameters of a porous structure. This work gives to ERT user's indications to establish or to evaluate the parameters used in the inversion. The surface conductivity of the grains was not considered in the present study, yet it may strongly influence the ERT measurement and the determination of the transport parameters (Monego et al. 2010; Revil and Florsch 2010); future work using our experimental setup filled with different type of grains together with complex resistivity measurement may help to better understand this issue.

Finally, we believe that our approach may be useful to test, validate and improve recent approaches such as coupled inversion (Pollock and Cirpka 2010) or stochastic methods (Revil and Jardani 2010). Future work will consider the influence of permeability heterogeneities, injection conditions and/or the stability of the displacement front and upscaling to the field scale with 3D modeling and stochastic inversion.

Acknowledgments

This article was significantly improved by the thoughtful reviews of André Revil, David Hart and an anonymous reviewer. The authors thank the University Paris-Sud for financial support (PPF "Modélisation des Processus Physique en Sciences de la Terre"). We thank R. Pidoux for realizing the experimental setup and A. Aubertin for the data acquisition program. We also thank Hermann Zeyen, Benoit Semin and Piotr Tucholka for helpful suggestions and discussions.

References

Bauer, P., R. Supper, S. Zimmermann, and W. Kinzelbach. 2006. Geoelectrical imaging of groundwater salinization in the Okavango Delta: Botswana. *Journal of Applied Geophysics* 60, no. 2: 126–141.

Batlle-Aguilar, J., S. Schneider, M. Pessel, P. Tucholka, Y. Coquet, and P. Vachier. 2009. Axisymetrical infiltration in soil imaged by noninvasive electrical resistivimetry. *Soil Science Society of America Journal* 73, no. 2: 510–520.

Bear, J. 1972. *Dynamics of Fluids in Porous Media*, 764 p. New York: American Elsevier.

Bevc, D., and H.F. Morrison. 1991. Borehole to surface electrical resistivity monitoring of a salt water injection experiment. *Geophysics* 56, no. 6: 769–777.

Binley, A., S. Henry-Poulter, and B. Shaw. 1996. Examination of solute transport in an undisturbed soil column using electrical resistance tomography. *Water Resources Research* 32, no. 4: 763.

Boschan, A., H. Auradou, I. Ippolito, R. Chertcoff, and J.P. Hulin. 2007. Miscible displacement fronts of shear thinning fluids inside rough fractures. *Water Resources Research* 43: W03438.

Cardarelli, E., and F. Fischanger. 2006. 2D data modelling by electrical resistivity tomography for complex subsurface geology. *Geophysical Prospecting* 54, no. 2: 121–133.

Daily, W., and E. Owen. 1991. Cross-borehole resistivity tomography. *Geophysics* 56, no. 8: 1228–1235.

Flowers, T.C., and J.R. Hunt. 2007. Viscous and gravitational contributions to mixing during vertical brine transport in water-saturated porous media. *Water Resources Research* 43: W01407.

Furman, A., T.P.A. Ferré, and G.L. Health. 2007. Spatial focusing of electrical resistivity surveys considering geologic and hydrologic layering. *Geophysics* 72, no. 2: F65–F73.

deGroot-Hedlin, C., and S. Constable. 1990. Occam's inversion to generate smooth two dimensional models from magnetotelluric data. *Geophysics* 55, no. 12: 1613–1624.

Johnson, T.C., P.S. Routh, T. Clemo, W. Barrash, and W.P. Clement. 2007. Incorporating geostatistical constraints in nonlinear inverse problems. *Water Resources Research* 43: W10422.

Kemna, A., J. Vanderborght, B. Kulessa, and H. Vereecken. 2002. Imaging and characterisation of subsurface solute transport using electrical resistivity tomography (ERT) and equivalent transport models. *Journal of Hydrology* 267, no. 3–4: 125–146.

Koestel, J., M. Javaux, R. Kasteel, A. Binley, and H. Vereecken. 2009. Imaging brilliant blue stained soil by means of electrical resistivity tomography. *Vadose Zone Journal* 8, no. 4: 963–975.

Labrecque, D.J., R. Sharpe, T. Wood, and G. Heath. 2004. Small-scale electrical resistivity tomography of wet fractured rocks. *Ground Water* 42, no. 1: 111–118.

Labrecque, D.J., A.L. Ramirez, W.D. Daily, A.M. Binley, and S.A. Schima. 1996. ERT monitoring of environmental remediation processes. *Measurement Science and Technology* 7, no. 3: 375–383.

Leroy, P., A. Revil, A. Kemna, P. Cosenza, and A. Ghorbani. 2008. Complex conductivity of water-saturated packs of glass beads. *Journal of Colloid and Interface Science* 321, no. 1: 103–117.

Lines, L.R., and S. Treitel. 1984. A review of least-squares inversion and its application to geophysical problems. *Geophysical Prospecting* 32, no. 2: 159–186.

Loke, M.H., and R.D. Barker. 1996. Rapid least-squares inversion of apparent resistivity pseudosections using a quasi-Newton method. *Geophysical Prospecting* 44, no. 1: 131–152.

Monego, M., G. Cassiani, R. Deiana, M. Putti, G. Passadore, and L. Altissimo. 2010. A tracer test in a shallow heterogeneous aquifer monitored via time-lapse surface electrical resistivity tomography. *Geophysics* 75, no. 4: WA61–WA73.

Nimmer, R.E., J.L. Osiensky, A.M. Binley, and B.C. Williams. 2008. Three-dimensional effects causing artefacts in two-dimensional cross-borehole electrical imaging. *Journal of Hydrology* 359, no. 1–2: 59–70.

Oldenborger, G.A., M.D. Knoll, P.S. Routh, and D.J. Labrecque. 2007. Time-lapse ERT monitoring of an injection/withdrawal experiment in a shallow unconfined aquifer. *Geophysics* 72, no. 4: F177–F187.

Olsen, P.A., A. Binley, and W. Tych. 1999. Characterizing solute transport in undisturbed soil cores using electrical and X-ray tomographic methods. *Hydrological Processes* 13: 211–221.

Pollock, D., and O.A. Cirpka. 2010. Fully coupled hydrogeophysical inversion of synthetic salt tracer experiments. *Water Resources Research* 46: W07501.

Pollock, D., and O.A. Cirpka. 2008. Temporal moments in geoelectrical monitoring of salt tracer experiments. *Water Resources Research* 44: W12416.

Peters, E.J., R. Gharbi, and N. Afzal. 1996. A look at dispersion in porous media through computed tomography imaging. *Journal of Petroleum Science and Engineering* 15: 23–31.

Revil, A., and N. Florsch. 2010. Determination of permeability from spectral induced polarization in granular media. *Geophysical Journal International* 181, no. 3: 1480–1498.

Revil, A., and A. Jardani. 2010. Stochastic inversion of permeability and dispersivities from time lapse self-potential measurements: a controlled sandbox study. *Geophysical Research Letters* 37: L11404.

Revil, A., and P.W.J. Glover. 1998. Nature of surface electrical conductivity in natural sands, sandstones, and clays. *Geophysical Research Letters* 25, no. 5: 691–694.

Seaton, W.J., and T.J. Burbey. 2002. Evaluation of two-dimensional resistivity methods in a fractured crystalline-rock terrane. *Journal of Applied Geophysics* 51, no. 1: 21–41.

Singha, K., and S.M. Gorelick. 2006. Hydrogeophysical tracking of three-dimensional tracer migration: The concept and application of apparent petrophysical relations. *Water Resources Research* 42: W06422.

Slater, L., A.M. Binley, W. Daily, and R. Johnson. 2000. Cross-hole electrical imaging of a controlled saline tracer injection. *Journal of Applied Geophysics* 44: 85–102.

Vanderborght, J., A. Kemna, H. Hardelauf, and H. Vereecken. 2005. Potential of electrical resistivity tomography to infer aquifer transport characteristics from tracer studies: a synthetic case study. *Water Resources Research* 41: W06013.

West, L.J., D.I. Stewart, A.M. Binley, and B. Shaw. 1999. Resistivity imaging of soil during electrokinetic transport. *Engineering Geology* 53, no. 2: 205–215.

Wilkinson, P.B., P.I. Meldrum, O. Kuras, J.E. Chambers, S.J. Holyoake, and R.D. Ogilvy. 2010. High Resolution Electrical Resistivity Tomography monitoring of a tracer test in a confined aquifer. *Journal of Applied Geophysics* 70, no. 4: 268–276.

Wolke, R., and H. Schwetlick. 1988. Iteratively reweighted least squares algorithms, converge analysis, and numerical comparisons. *SIAM Journal of Science and Statistical Computing* 9, no. 5: 907–921.